



NRC Publications Archive Archives des publications du CNRC

Vibrational spectroscopy and thermophysical properties of ultralow sulfur diesel: alternative fuel binary blends

Petrucci, Thiago; Michaelian, Kirk H.; Gieleciak, Rafal; Shen, Jun; Zhou, Jianqin; Gu, Caikang; Neill, W. Stuart; Baesso, Mauro L.; Malacarne, Luis C.; Astrath, Nelson G. C.

This publication could be one of several versions: author's original, accepted manuscript or the publisher's version. / La version de cette publication peut être l'une des suivantes : la version prépublication de l'auteur, la version acceptée du manuscrit ou la version de l'éditeur.

For the publisher's version, please access the DOI link below. / Pour consulter la version de l'éditeur, utilisez le lien DOI ci-dessous.

Publisher's version / Version de l'éditeur:

<https://doi.org/10.1021/acs.energyfuels.7b02847>

Energy & Fuels, 31, 12, pp. 13775-13784, 2017-11-28

NRC Publications Record / Notice d'Archives des publications de CNRC:

<https://nrc-publications.canada.ca/eng/view/object/?id=20891c80-22c2-4dd4-9396-d347b2c50ed2>

<https://publications-cnrc.canada.ca/fra/voir/objet/?id=20891c80-22c2-4dd4-9396-d347b2c50ed2>

Access and use of this website and the material on it are subject to the Terms and Conditions set forth at

<https://nrc-publications.canada.ca/eng/copyright>

READ THESE TERMS AND CONDITIONS CAREFULLY BEFORE USING THIS WEBSITE.

L'accès à ce site Web et l'utilisation de son contenu sont assujettis aux conditions présentées dans le site

<https://publications-cnrc.canada.ca/fra/droits>

LISEZ CES CONDITIONS ATTENTIVEMENT AVANT D'UTILISER CE SITE WEB.

Questions? Contact the NRC Publications Archive team at

PublicationsArchive-ArchivesPublications@nrc-cnrc.gc.ca. If you wish to email the authors directly, please see the first page of the publication for their contact information.

Vous avez des questions? Nous pouvons vous aider. Pour communiquer directement avec un auteur, consultez la première page de la revue dans laquelle son article a été publié afin de trouver ses coordonnées. Si vous n'arrivez pas à les repérer, communiquez avec nous à PublicationsArchive-ArchivesPublications@nrc-cnrc.gc.ca.



Vibrational Spectroscopy and Thermophysical Properties of Ultralow Sulfur Diesel—Alternative Fuel Binary Blends

Thiago Petrucci,^{†,‡} Kirk H. Michaelian,[†] Rafal Gieleciak,[†] Jun Shen,^{*,§,¶} Jianqin Zhou,[§] Caikang Gu,[§] W. Stuart Neill,^{||} Mauro L. Baesso,[‡] Luis C. Malacarne,^{‡,¶} and Nelson G. C. Astrath[‡]

[†]Natural Resources Canada, CanmetENERGY—Devon, One Oil Patch Drive, Devon, Alberta T9G 1A8, Canada

[§]National Research Council Canada, Energy, Mining and Environment Research Center, 4250 Wesbrook Mall, Vancouver, British Columbia V6T 1W5, Canada

^{||}National Research Council Canada, Energy, Mining and Environment Research Center, 1200 Montreal Road, Building M-9, Ottawa, Ontario K1A 0R6, Canada

[‡]Departamento de Física, Universidade Estadual de Maringá, Avenue Colombo 5790, Maringá, Paraná 87020-900, Brazil

Supporting Information

ABSTRACT: Four alternative fuels (AF) were blended with ultralow sulfur diesel (ULSD) at five different proportions (10, 20, 30, 50, and 100 vol % AF) to create 20 binary mixtures in this work. Two renewable jet AFs and two renewable diesel AFs were investigated. Interactions between the components in the mixtures were analyzed by means of spectroscopy (Raman, near-infrared), thermophysical (thermal diffusivity, thermo-optic coefficient), and physical (density) techniques. Correlations among the data were investigated using principal component analysis and partial least-squares regression. Trends in Raman intensities and band positions as well as thermophysical properties showed that the AF/ULSD blends resembled two-component mixtures despite the known complexities of the constituents. Specifically, spectra combined according to the percentages of the components in each mixture; thermophysical and physical properties exhibited similar behavior. The spectra showed strong correlations with all three physical properties, creating the possibility for predicting the properties of similar AF/ULSD mixtures. These properties are governed by the chemical compositions of the fuels.

1. INTRODUCTION

The cost, availability, and accessibility of fuel have a major impact on the operating, planning, and development of the transportation industry. For example, many commercial airline and oil-refining and marketing companies favor the increased utilization of renewable feedstock-based fuels or blends to reduce dependence on a single (fossil fuels) energy source, mitigate greenhouse gas emissions, and reduce vulnerability to the instabilities of petroleum prices.¹ Currently, there are many process technologies that convert biomass-based materials (e.g., waste fats, oils, and greases, as well as industrial oil crops and algae) into drop-in renewable and alternative fuels (AF), the most advanced being Fischer–Tropsch biomass-to-liquid (FT BTL) synthesis, hydroprocessed renewable jet (HRJ), alcohol-to-jet (ATJ), oil-to-jet (OTJ), gas-to-jet (GTJ), and sugar-to-jet (STJ).²

Not every synthetic fuel production pathway creates the hydrocarbon types that are needed to meet fuel specifications. Generally, AFs should be fully miscible with conventional fuels because of the requirement for blending, and they should be compatible with existing fuel infrastructure.² Most AFs contain hydrocarbon species similar to those that exist in petroleum-based fuels, such as paraffins, isoparaffins, naphthenes, and aromatics. The most important differences between AFs and conventional fuels exist in the relative concentrations and boiling point distributions of their hydrocarbon species. These dissimilarities can affect the physical and chemical properties as well as combustion and emission performance of AFs in engine

tests.^{3,4} It can be noted that some AFs comprise mostly one type of species, distributed across a wide boiling point range.⁵ AFs also tend to have fewer contaminants such as sulfur and nitrogen.

Hydrocarbon distillate fuels were characterized by means of Raman spectroscopy and photothermal techniques in a recent study in our laboratory.⁶ Two thermophysical properties, thermal diffusivity (D) and the thermo-optic coefficient (dn/dT), were shown to be related to several chemical and physical properties of the fuels and to ignition quality. D is the ratio of thermal conductivity to volumetric heat capacity, quantifying the conduction of thermal energy relative to its storage. dn/dT (also known as the temperature coefficient of the refractive index) represents the competition between polarizability and thermal expansion of a material, conveying information about molecular size; because this quantity is negative for petroleum fuels or hydrocarbon mixtures, $-dn/dT$ data were reported. Fuels with lower cetane numbers, lower distillation temperatures, and lower kinematic viscosities had greater $-dn/dT$ values; by contrast, $-dn/dT$ was smaller for larger hydrocarbon molecules. The present investigation expands upon this research, including near-infrared (NIR) spectroscopy as an additional method of analysis. Moreover, D was measured by an alternative technique in the current work.

Received: September 20, 2017

Revised: November 22, 2017

Published: November 28, 2017

Table 1. Selected Properties of the ULSD Fuel and Alternative Fuel (AF) Blending Components

fuel property	ASTM method	ULSD	AF1	AF2	AF3	AF4
density (g/cm ³ , 15 °C)	D4052	0.8347	0.7566	0.8041	0.7789	0.7781
kinematic viscosity (cSt, 40 °C)	D445	2.140	1.323	1.257	2.575	2.636
derived cetane no.	D6890	43.1	56.4	57.1	70.9	73.0
IBP (°C)	D86	164	144	152	163	150
T10	D86	185	159	168	226	223
T50	D86	236	206	202	280	282
T90	D86	315	273	248	294	294
FBP	D86	355	281	267	307	306

This investigation had two main goals. The first goal was to analyze a series of binary alternative fuel/ultralow sulfur diesel (AF/ULSD) blends using Raman and NIR spectroscopies to elucidate compositions and interactions between the components. The second objective was to identify relationships among the thermophysical properties and among the spectra for these blends. Another physical property, density (ρ), was examined together with D and $-dn/dT$. Principal component analysis (PCA) and partial least-squares regression (PLSR) facilitated and enhanced the interpretation of the spectroscopy data and their relationships with the thermophysical parameters. The results from these numerical methods confirmed the existence of important relationships based on the different compositions of the AFs and ULSD. Raman and NIR spectroscopies as well as the optical and photothermal methods were found to provide essential information on the characteristics of the AF/ULSD blends.

2. EXPERIMENTAL SECTION

2.1. Samples. The fuel samples were prepared by blending alternative renewable components with an ultralow sulfur diesel (ULSD) fuel. The ULSD fuel was a Canadian commercial diesel fuel derived from oil sands sources. The alternative fuels consisted of two renewable jet (AF1 and AF2) and two commercial, renewable diesel (AF3 and AF4) blending components. Selected properties of the ULSD and alternative fuels are provided in Table 1. Two of the alternative fuels (AF3 and AF4) were prepared by lightly hydrotreating vegetable oils or waste fats to produce a paraffinic fuel. AF1 was produced by hydroprocessing vegetable oils or waste fats to produce a paraffinic fuel in the jet fuel boiling range, which was then isomerized to improve the low-temperature properties. The final alternative fuel (AF2) was prepared by catalytic hydrothermolysis of a vegetable oil, which produced paraffins, naphthenes, and aromatics. The fuel properties, except for derived cetane number, were measured by InnoTech Alberta. The derived cetane numbers were measured by National Research Council Canada.

The fuel samples were divided into four groups as shown in Table 2. The four alternative fuels were blended with the ULSD fuel in five different proportions (10, 20, 30, 50, and 100 vol % AF; 90, 80, 70, 50, and 0 vol % diesel, respectively). The five blends for the four fuels produced 20 mixtures, which were identified according to the scheme in Table 2 for this investigation. The liquids were stored in plastic containers in a freezer below -10 °C to prevent chemical changes and evaporation.

2.2. Raman Spectroscopy. FT-Raman spectra were obtained at 4 cm⁻¹ resolution using a Bruker IFS 88 Fourier Transform Infrared (FT-IR) spectrometer and an FRA 106 Raman accessory. The spectrometer was equipped with a Si/CaF₂ beamsplitter. An air-cooled, diode-pumped 1064.5 nm Nd:YAG laser was employed for excitation. Fuel samples were held in a 5 mm mirrored quartz cuvette, and the Raman-scattered light was collected using a backscattering geometry. Fifteen 50-scan double-sided interferograms were averaged prior to calculation of each spectrum.

2.3. Near-Infrared Spectroscopy. NIR spectra were recorded by use of the same IFS 88 spectrometer. A tungsten lamp served as the

Table 2. Sample Composition and Numbering

alternative fuel ^a	sample no.	percent biofuel	percent diesel
AF1	1	10	90
	2	20	80
	3	30	70
	4	50	50
	5	100	0
AF2	6	10	90
	7	20	80
	8	30	70
	9	50	50
	10	100	0
AF3	11	10	90
	12	20	80
	13	30	70
	14	50	50
	15	100	0
AF4	16	10	90
	17	20	80
	18	30	70
	19	50	50
	20	100	0
ULSD	21	0	100

^aAlternative fuels (AF_{*n*}) contained 90 ppm of a commercial lubricity additive.

radiation source. The spectrometer was purged with dry nitrogen to minimize absorption by atmospheric water vapor and CO₂. The liquid samples were held in a 50 μ m cell fitted with CaF₂ windows. Spectra were acquired at a resolution of 6 cm⁻¹. A spectrum of the empty cell served as the reference (background) for calculation of transmittance spectra. The region above 4600 cm⁻¹, where absorbance did not exceed 1.0, was analyzed in detail in this work.

2.4. Thermophysical and Optical Measurements. The thermal wave resonant cavity (TWRC) apparatus described in ref 7 was employed to measure the thermal diffusivities of the samples. Radiation from a 532.0 nm laser (Melles Griot, model 58 GLS/GSS 301, 30 mW) was modulated at 2.599 Hz by a mechanical chopper (Boston Electronics, model CH-60) and arranged to impinge on a surface-blackened 22 μ m thick aluminum foil within the TWRC to generate the thermal wave. A 100 μ m thick polyvinylidene fluoride (PVDF) film produced the TWRC signal, which was transmitted to a low-noise preamplifier (Stanford Research Systems, model SR 560) and detected by a lock-in amplifier (EG&G, model 7260). The aluminum foil–PVDF distance was varied using a precision linear stage (Physik Instrumente, model PLS-8S, 1 μ m resolution). These cavity-length scans were performed with the fuel blends as intracavity samples. It can be noted that the laser beam does not contact the sample directly in the TWRC, thereby obviating the possibility of photochemical reactions like those observed with the alternative thermal lens technique in our previous study.⁶

A Fabry–Perot interferometer, depicted in ref 8, was used to determine the thermo-optic coefficients for the fuel blends. Samples

were contained in a quartz cuvette ($L = 10$ mm) and irradiated by a weak (5 mW) He–Ne laser beam ($\lambda = 632.8$ nm). Multiple reflections at both inner surfaces of the cuvette created a pattern of interference fringes. These fringes were detected by a photodiode, with their intensities being measured by a voltmeter (Agilent 34401A 61/2 Digit Multimeter). Slow, uniform resistive heating of the cuvette caused the fringes to move. Peak analysis was performed, where each temperature T corresponding to a signal peak was extracted and correlated with the interference order m to obtain an m – T curve and its derivative dm/dT . The thermo-optic coefficient was then determined using the relation $dn/dT = (\lambda/2L)(dm/dT)$.

2.5. Density. Densities of the fuel blends were measured at 25 °C using an Anton Paar density meter, model 4500. The measuring cell was cleaned and flushed with dry air before each analysis. Air bubbles were excluded from the samples before the density measurements. Nominal repeatability was about 1×10^{-5} g/cm³ for density and 0.01 °C for temperature. Series of repeated measurements indicated that the uncertainties of the density measurements were $\pm 3 \times 10^{-5}$ g/cm³. The reported density values were rounded to four significant figures.

2.6. Multivariate Analysis. Principal component analysis (PCA)⁹ was employed to examine the potential relationships among the Raman and NIR spectra of the fuel blends. PCA is a well-established statistical method to extract the systematic variance from a large data set into a few coherent parameters called principal components (PCs). Two types of data pretreatment were performed prior to PCA. The Raman spectra were mean centered, whereas the NIR spectra were baseline linearized (“background corrected”) and also mean centered. Scores and loadings were calculated after these pretreatment steps.

Partial least-squares regression (PLSR)¹⁰ was used to develop models linking the information contained in both types of spectra with that in the thermophysical and properties (D , $-dn/dT$) and the density (ρ). PLSR models were constructed for pretreated data, with both model complexity and internal predictivity being estimated by means of the leave-one-out cross-validation (CV) procedure.¹¹ A series of 17 samples containing different AF percentages was selected as the training set. The test set comprised samples 1, 7, 13, and 19 (one from each AF group and each biofuel percentage). In the final step of this analysis, the properties predicted by the models were compared with the experimental values for D , $-dn/dT$, and ρ . Multivariate data analysis was performed using Origin (OriginLab) and Matlab (2012b; The MathWorks) software.

3. RESULTS AND DISCUSSION

3.1. Thermophysical Properties. Experimental results for D , $-dn/dT$, and ρ are summarized in Table 3, together with uncertainties estimated from at least five consecutive measurements for each of the two thermophysical properties. The relationships among the three quantities are illustrated in Figure 1. In all three panels two particular phenomena are apparent. First, each panel illustrates a set of linear relations between two properties as the AF n concentrations vary from 10% to 100%; in each case the fitted lines converge to the corresponding ordinate for ULSD (sample 21), where the AF percentages all become zero. Second, the data points for the respective AF3/ULSD and AF4/ULSD blends fall close together at each percentage (10, 20, 30, 50, and 100) in all three plots. This observation suggests that AF3 and AF4 are similar to each other with regard to their chemical makeup. D and ρ vary more rapidly than $-dn/dT$ for AF3 and AF4, in contrast with the results for AF1 and AF2. Although other fuel properties of these blends are not available, the correlations among the thermophysical properties ($-dn/dT$ and D), distillation temperatures (T10, T50, and T90), kinematic viscosity, and derived cetane number are expected to be similar to those reported in ref 6.

If Figure 1a is considered in isolation (in other words, only the two thermophysical properties are compared), one might

Table 3. Experimental Values for Thermo-Optic Coefficient ($-dn/dT$), Thermal Diffusivity (D), and Density (ρ).

sample no.	$-dn/dT$ (10^{-4} K ⁻¹)	D (10^{-8} m ² s ⁻¹)	ρ (g/cm ³) ^a
1	4.09 ± 0.01	7.02 ± 0.02	0.8210
2	4.11 ± 0.01	7.05 ± 0.02	0.8130
3	4.124 ± 0.003	7.10 ± 0.04	0.8061
4	4.17 ± 0.01	7.18 ± 0.04	0.7909
5	4.263 ± 0.003	7.39 ± 0.03	0.7516
6	4.09 ± 0.01	7.04 ± 0.02	0.8255
7	4.118 ± 0.003	7.08 ± 0.03	0.8228
8	4.15 ± 0.01	7.14 ± 0.03	0.8200
9	4.19 ± 0.01	7.25 ± 0.03	0.8145
10	4.301 ± 0.003	7.54 ± 0.02	0.7999
11	4.062 ± 0.003	7.06 ± 0.02	0.8228
12	4.06 ± 0.01	7.14 ± 0.03	0.8173
13	4.062 ± 0.003	7.19 ± 0.04	0.8116
14	4.06 ± 0.01	7.34 ± 0.02	0.8006
15	4.03 ± 0.01	7.73 ± 0.02	0.7731
16	4.068 ± 0.003	7.06 ± 0.03	0.8204
17	4.06 ± 0.02	7.11 ± 0.03	0.8170
18	4.058 ± 0.003	7.23 ± 0.02	0.8113
19	4.055 ± 0.003	7.36 ± 0.03	0.8002
20	4.02 ± 0.01	7.79 ± 0.02	0.7722
21	4.074 ± 0.003	6.99 ± 0.03	0.8282

^aUncertainties of the density measurements were $\pm 3 \times 10^{-5}$ g/cm³. The reported density values were rounded to four significant figures.

conclude that there are just two groups of fuels: (AF1, AF2) and (AF3, AF4). However, the introduction of density as an additional physical property (middle and lower panels) provides discrimination between AF1 and AF2; for example, one can observe that AF2 is denser than AF1. This suggests that these two fuels likely have different compositions.

To summarize, although detailed conclusions regarding the chemical compositions of the fuels cannot be discerned from Figure 1, the thermophysical data convey important information regarding several similarities (and differences) among these compositions. The alternative fuels fall into three groups, a classification that is supported by the spectroscopy data discussed below. Moreover, the linear trends in this figure suggest that the AF/ULSD blends resemble simple two-component mixtures, an approach that also accords with the Raman and NIR spectra.

3.2. Raman Spectroscopy. Survey Raman spectra of AFs 5, 10, 15 and 20 as well as ULSD are presented in Figure 2. As might be expected, these spectra are generally similar to those obtained previously in our laboratory for middle distillate fuels as well as numerous distillation fractions and process samples.^{12,13} The prominent features at about 1375, 1450, and 2800–3000 cm⁻¹ are mostly due to alkyl (CH₂ and CH₃) groups. At lower wavenumbers several weaker bands signify the presence of various well-known functional groups. A narrow peak near 1000 cm⁻¹ and another band at ~1600 cm⁻¹ show that AF2 and ULSD contain aromatic functionality; these features are discussed in more detail below. No significant bands appear between approximately 1700 and 2700 cm⁻¹.

The overlapping, more intense carbon–hydrogen stretching bands are shown in greater detail in the inset. These bands provide information on the branching of alkyl chains and on the distinctions among the AFs mentioned in the previous section. Four vibration types are associated with the principal maxima (locations rounded to the nearest five-wavenumber interval)

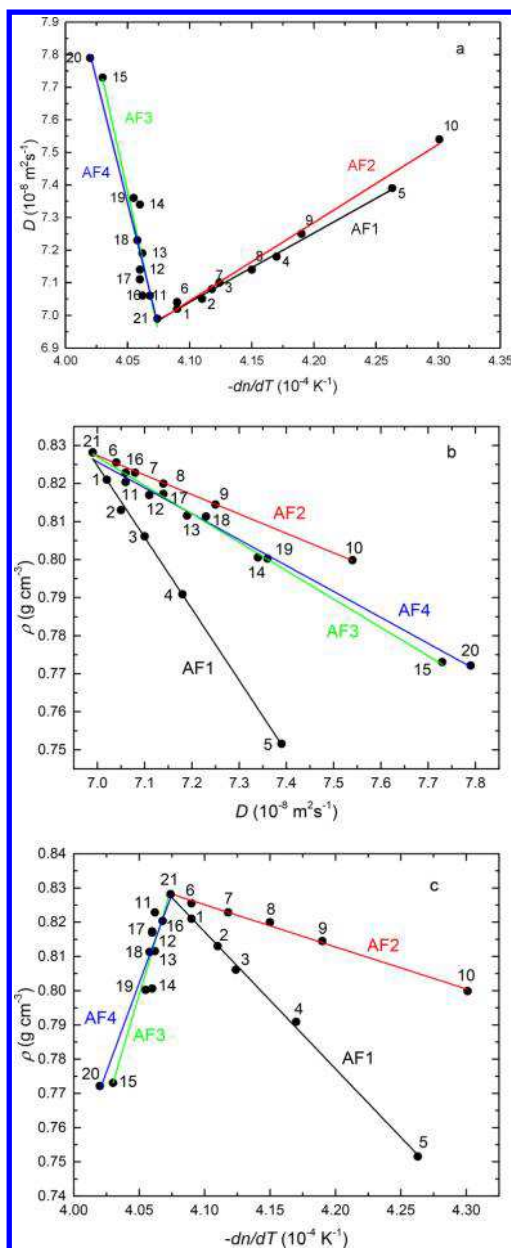


Figure 1. Relationships among thermophysical properties D (thermal diffusivity), $-dn/dT$ (thermo-optic coefficient), and ρ (density) for the 21 samples studied in this work.

visible in this figure: 2850 cm^{-1} , CH_2 symmetric stretch; 2870 cm^{-1} , CH_3 symmetric; $2915\text{--}2930\text{ cm}^{-1}$, CH_2 asymmetric; 2960 cm^{-1} , CH_3 asymmetric. Inspection of the figure reveals that both CH_2 bands are relatively weak for AF1, while the CH_3 bands are prominent. This preponderance of terminal CH_3 groups suggests a majority of short alkyl chains. For AF2 the situation is reversed: the CH_2 bands are stronger and the CH_3 features are diminished. Hence, greater chain lengths can be inferred for this fuel.

Results for AF3, AF4, and ULSD are more complex. The symmetric and asymmetric stretching bands do not exhibit like behavior in the spectra of any of these three samples, making conclusions similar to those in the previous paragraph impossible. In fact, the latter type of situation is fairly common in Raman and infrared spectra of various hydrocarbon fuels.^{12,13} Notwithstanding this result, it is readily apparent that the

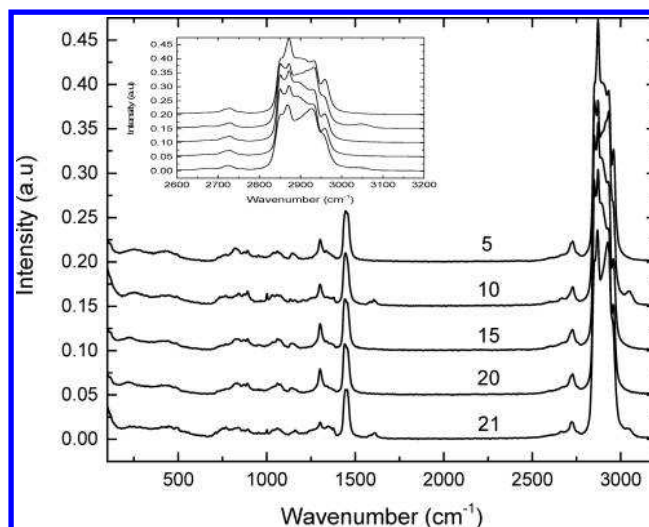


Figure 2. Raman spectra of alternative fuels 5, 10, 15, and 20, in addition to ULSD (sample 21). Curves are displaced vertically by successive 0.05 intensity increments (arbitrary scale) for clarity. (Inset) Expanded view of C–H stretching region, $2600\text{--}3200\text{ cm}^{-1}$.

spectra of AF3 and AF4 in this figure are practically identical—a finding reminiscent of the relationships among the thermophysical properties of these two fuels in Figure 1. Thus, the Raman spectra confirm that the AFs fall into three groups: (a) AF1, (b) AF2, and (c) AF3 and AF4.

Figure 3 provides still another perspective on the C–H stretching region. The Raman spectra acquired for samples 1–

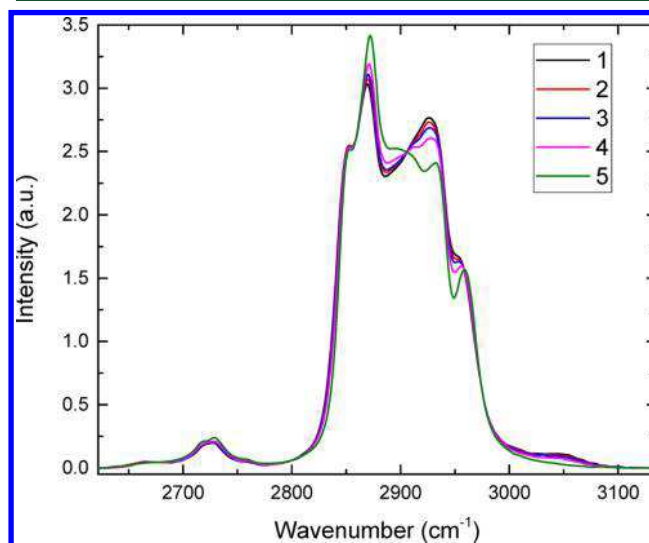


Figure 3. Baseline-linearized CH stretching region of Raman spectra for samples 1–5.

5, in which the AF1 fraction ranges from 10% to 100% (Table 2), have been baseline linearized and normalized with respect to the integrated area in this figure. A well-defined isosbestic (equal intensity) point is visible at 2906 cm^{-1} . Further examination reveals two additional isosbestic points at 2860 cm^{-1} (CH_2/CH_3 symmetric stretch) and 2959 cm^{-1} (CH_3 asymmetric stretch). For samples 6–10, similar points occur at 2845 , 2862 , 2906 , 2931 , and 2942 cm^{-1} . AF3 and AF4 share isosbestic points at 2844 and 2906 cm^{-1} . Hence, the 2906 cm^{-1} ordinate is common in all of the spectra; effectively, Raman

intensity is equal for AF1–4 and ULSD at this wavenumber. Bands in this region are generally attributed to aliphatic CH (distinguished from CH_2 and CH_3) groups; this leads to the interesting proposal that the abundance of CH functionality is approximately constant in the studied fuels. The equal-intensity points observed in this work are qualitatively similar to those observed by Corsetti et al. in infrared and Raman spectra of ethanol/gasoline blends,^{14,15} although slightly different locations were noticed in those spectra. In the present Raman study of AF/ULSD blends, the existence of isosbestic points accords with the suggestion that each blend acts essentially as a mixture of two compounds, despite the known complexities of the fuels. Plots of the C–H stretching region for the blends derived from AF2, AF3, and AF4 are included in the [Supporting Information](#).

3.2.1. Curve Fitting. It is readily apparent that the C–H stretching region in the spectra of the AF/ULSD blends is comprised of several component bands and that the relative intensities of these bands vary significantly according to the AF/ULSD ratio ([Figure 3](#)). To characterize the spectra in more detail, curve-fitting calculations were performed for all of the 21 samples studied in this work. Representative results obtained for ULSD are shown in [Figure 4a](#). It is observed that a satisfactory fit results from the use of six aliphatic (~ 2800 – 3000 cm^{-1}) bands, together with one additional band in the aromatic region (~ 3000 – 3100 cm^{-1}). Lorentzian band shapes were assumed for convenience in this calculation. This seven-band model is based on the curve-fitting strategies utilized previously in our laboratory for light and heavy gas oil distillation fractions.^{12,13} The fitted bands (locations rounded to the nearest wavenumber) are assigned to CH_n stretching vibration types according to the values given previously: 2849 cm^{-1} , CH_2 symmetric; 2868 cm^{-1} , CH_3 symmetric; 2893 cm^{-1} , CH; 2913 and 2932 cm^{-1} , CH_2 asymmetric; 2958 cm^{-1} , CH_3 asymmetric. The much weaker aromatic CH band is located at 3048 cm^{-1} .

Comparison of the calculation results for each set of five blends quickly reveals that the frequencies of the individual aliphatic CH_n bands are not constant: in most cases the frequencies vary monotonically between their values for 100% AF n and 100% ULSD as the AF n /ULSD ratio changes. A typical example, pertaining to the AF1 sample set, is presented in [Figure 4b](#). The CH_2 symmetric stretching frequency shifts in an approximately linear fashion from 2850.9 (sample 5, 100% AF1) to 2848.8 cm^{-1} (100% ULSD). This behavior implies additivity of the AF1 and ULSD spectra for samples 1–5. Similar results were observed for most of the other aliphatic C–H bands, although the results for the ~ 2893 and 2913 cm^{-1} bands sometimes were irregular. Poorer fits were sometimes obtained in this intermediate region, which incidentally includes the common 2906 cm^{-1} isosbestic point mentioned above. Curve-fitting results for the 20 AF n /ULSD blends, the positions of the fitted bands, and plots showing the variations in these positions with AF n /ULSD ratios are included in the [Supporting Information](#). It should be noted that the aromatic C–H band did not exhibit any systematic frequency trends.

3.2.2. Principal Component Analysis. [Figure 2](#) shows that the fingerprint regions of the Raman spectra of the AFs and ULSD are, in general, quite similar. Before PCA of the spectra is described, a comment on two specific features is appropriate. As alluded to earlier, careful inspection reveals bands due to monocyclic aromatics ($\sim 1000\text{ cm}^{-1}$) and total aromatics ($\sim 1600\text{ cm}^{-1}$) in the AF2 and ULSD data. Similar assignments of these aromatic bands in Raman spectra of distillation

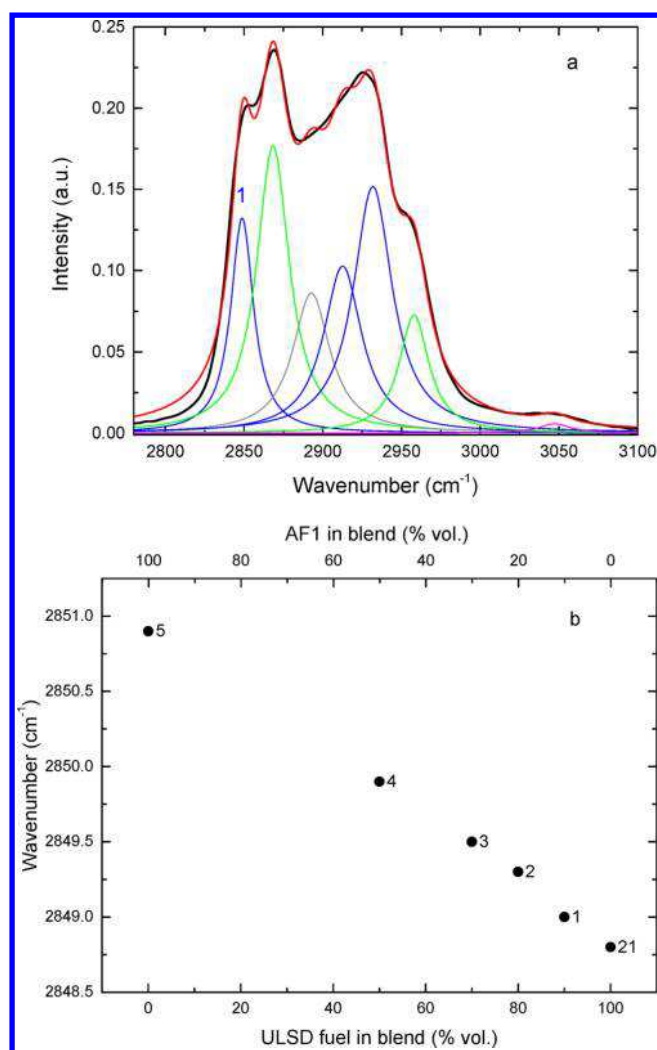


Figure 4. (a) Curve-fitting result for the CH stretching region of the ULSD spectrum: (black curve) original spectrum; (red) fitted spectrum; (blue) CH_2 groups; (green) CH_3 ; (gray) CH; (magenta) aromatic CH. Band assignments are discussed in the text. (b) Positions for band 1 (labeled) in spectra of samples 1–5 and 21.

fractions were discussed in our previous work.^{12,13} At higher wavenumbers, the C–H stretching region provides additional important information: the spectra of AF3 and AF4 are very similar to each other but distinct from those for AF1 and AF2. The existence of a weak band near 3050 cm^{-1} affirms the presence of aromatic CH groups in AF2 and ULSD. Two-dimensional gas chromatography studies of the fuels carried out in our laboratory (not presented in this work) also confirm the existence of aromatic species in AF2 and ULSD.

To enhance and extend this interpretation of the spectra, PCA was carried out for both the fingerprint and the C–H stretching regions. As noted in [section 2.5](#), the spectra were mean centered as a preprocessing step prior to the PCA calculations. The intervening portion from 1700 to 2660 cm^{-1} was not analyzed because it primarily contains noise, with no obvious features of interest.

The PCA scores plot for all 21 Raman spectra is shown in [Figure 5](#). The four AF groups fall into three areas: labeled A, B, and C. The calculated variances for PC1 and PC2 were 77.26% and 14.65%, respectively, together accounting for 91.9% of the total variance in the data. The AF3 and AF4 data (region B)

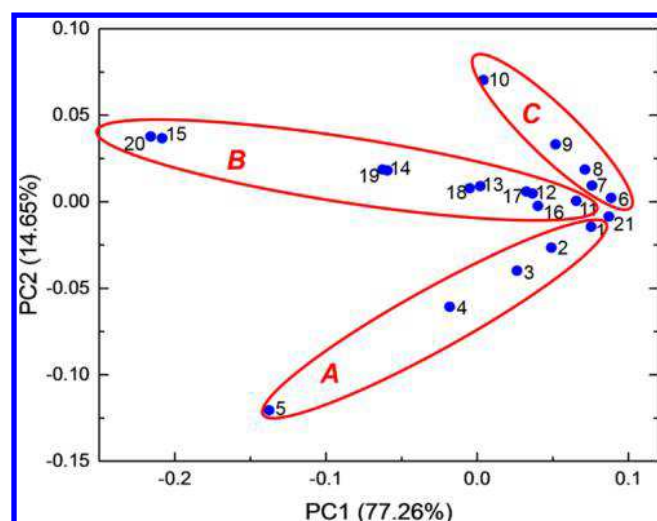


Figure 5. Scores plot using the first two principal components for the Raman spectra. Regions indicate fuel sets: A (samples 1–5); B (samples 11–15 and 16–20); C (samples 6–10).

occur together, a consequence of the close similarity of these fuels (see above). The AF1 and AF2 blends present different values for PC2, with each falling into its own region (A and C, respectively). For the first principal component, the AF2 samples and ULSD exhibit only positive values. By contrast the AF1, AF3, and AF4 blends are located in both positive and negative regions for PC1. The AF n blends show different scattering profiles for PC2. AF2, AF3, and AF4 blends are located in the positive part of the scores plot, whereas the AF1 blends and ULSD fall in the negative area. Stated differently, PC1 can be thought to represent concentration/composition because this axis shows differences among the samples according to their AF n /ULSD ratios. On the other hand, PC2 can be interpreted as referring to hydrocarbon type because its axis illustrates differences among aromatic (AF2, ULSD) and nonaromatic (AF1, AF3, AF4) fuels.

The results in Figure 5 were obtained using both 400–1700 and 2660–3110 cm^{-1} Raman data. In a slightly different approach, PCA was next performed for these two intervals individually. Loadings plots for the first two PCs in the fingerprint and C–H stretching regions are presented in Figures 6 and 7, respectively. The spectra of the four AFs (also shown in Figure 2) are included for comparison with the PCs. The loadings plots represent the weight of each variable (wavenumber) associated with the PCs and describe the contribution of a given variable during construction of the particular PCs. The variances calculated using the fingerprint or C–H regions separately or both regions together are quite similar for the first four PCs. This implies that the fingerprint and C–H stretching regions of the Raman spectra convey roughly equivalent information regarding the chemical compositions of the fuel blends—a significant result that could potentially guide future investigations of similar blends.

3.2.3. Multivariate Calibration. It is desirable to establish and characterize the relationships that exist between the Raman spectra and each of the thermophysical properties for the AFs. These links are of interest since, in favorable cases, they can make it possible to predict the properties for additional samples if only their Raman spectra are available. In this work PLSR was utilized to investigate the spectroscopy/thermophysical property relationships. Four factors were sufficient for this

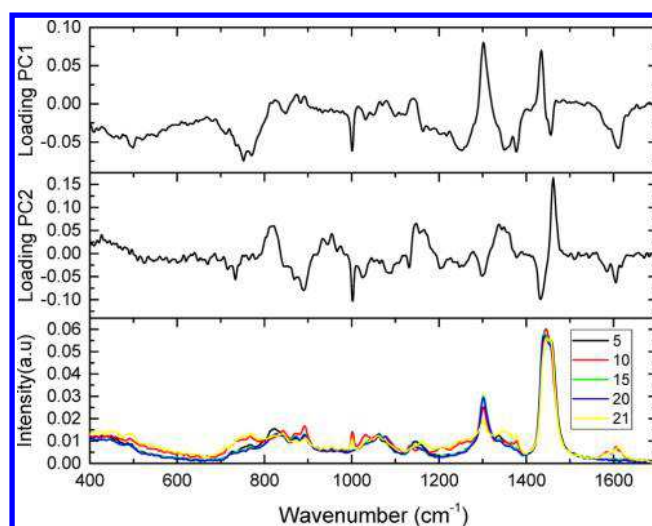


Figure 6. Fingerprint region of Raman spectra for samples 5, 10, 15, 20, and 21: (top) PC1; (middle) PC2; (bottom) spectra.

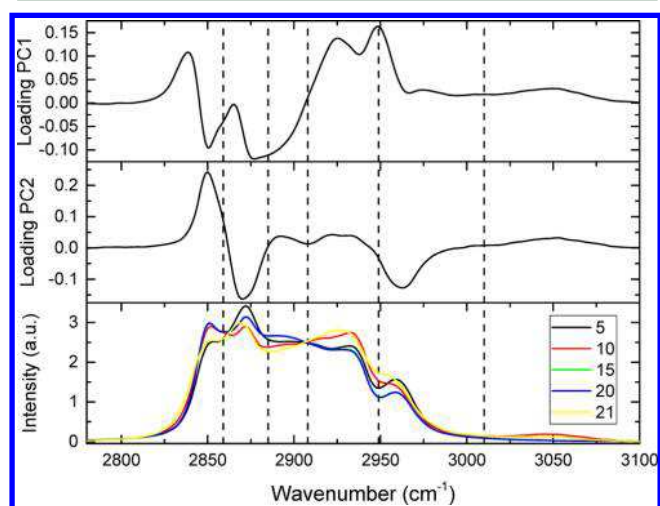


Figure 7. CH stretching region of Raman spectra for samples 5, 10, 15, 20, and 21: (top) PC1; (middle) PC2; (bottom) baseline-linearized spectra. Dashed lines demarcate vibration types: 2780–2859 cm^{-1} , CH_2 symmetric; 2859–2885 cm^{-1} , CH_3 symmetric; 2885–2908 cm^{-1} , CH ; 2908–2949 cm^{-1} , CH_2 asymmetric; 2949–3010 cm^{-1} , CH_3 asymmetric; 3010–3100 cm^{-1} , aromatic CH .

calculation, as was determined through calculations of the predicted residual error sum of squares.

The two spectrum regions mentioned earlier were used independently, and also together, for the PLSR calculations. It turns out that the agreement between the actual (i.e., experimental) and the predicted values for D , $-dn/dT$, and ρ is essentially the same when data from either or both regions are utilized. Results obtained using 400–1700 cm^{-1} data (variance = 96.4%) are presented in Table 4. The close agreement among the various calculation strategies again suggests that the information contained in the fingerprint region of the Raman spectra is, practically speaking, equivalent to that in the C–H stretching region. Accordingly, measurement and numerical analysis of the entire Raman spectra from 400 to 3110 cm^{-1} is not essential for prediction of the thermophysical properties. It is appropriate to mention that this conclusion is based on an investigation involving a limited number of samples; clearly, further work involving significantly

Table 4. Actual and Predicted Values for D , $-dn/dT$, and ρ Based on 400–1700 cm^{-1} Raman Data

sample	D_{actual} ($10^{-8} \text{ m}^2 \text{ s}^{-1}$)	$D_{\text{predicted}}$ ($10^{-8} \text{ m}^2 \text{ s}^{-1}$)	dn/dT_{actual} (10^{-4} K^{-1})	$dn/dT_{\text{predicted}}$ (10^{-4} K^{-1})	ρ_{actual} (g cm^{-3})	$\rho_{\text{predicted}}$ (g cm^{-3})
1	7.02	7.01	4.09	4.10	0.821	0.820
7	7.08	7.08	4.12	4.13	0.823	0.822
13	7.19	7.21	4.06	4.06	0.812	0.811
19	7.36	7.37	4.06	4.07	0.800	0.799

larger numbers would be required to confirm the conclusions reached so far.

3.3. Thermophysical and Spectroscopic Additivity.

The results described in the preceding paragraphs consistently indicate the additive natures of the Raman spectra and thermophysical properties for the investigated fuel set. Further consideration of these spectra leads to the suggestion that another type of additivity could exist with regard to intensities. In particular, the spectra of a specific AF n and the ULSD should combine according to the percentages of these two components in a given blend. This predicted additivity is most easily investigated for the strong bands in the 2800–3000 cm^{-1} region, rather than the weaker features at lower wavenumbers. In fact, each sum of the spectra for ULSD and an AF n , calculated by scaling these two spectra according to the percentages in Table 2, was found to be practically identical to the experimental spectrum for the blend in question. These observations confirm the additivity of the Raman spectra of the AF n /ULSD blends.

Figure 8 illustrates similar comparisons for both thermophysical properties and density. Experimental and predicted $-dn/dT$ values are shown for all 21 samples in the upper panel, with a similar comparison for D and ρ being displayed in the middle and bottom panels, respectively. All investigated properties show good agreement for each pair of data, the differences naturally falling to zero for samples 5, 10, 15, and 20 (AF 1, 2, 3, and 4, respectively). Trends within each set of five samples, which have origins analogous to those observed in Figure 1, are clearly visible in Figure 8. Additivities of the thermophysical properties for the AF n /ULSD blends are thus confirmed. In this context, it is relevant to mention that previous studies in our laboratory also demonstrated the additive behavior of the thermo-optic coefficients of simple liquid hydrocarbons in both binary and complex mixtures.^{16,17} As shown in Table 3, the standard deviations are less than 0.3% and 0.6% of the mean values of $-dn/dT$ and D , respectively. Therefore, the standard deviations are not presented in Figure 8.

3.4. Near-Infrared Spectroscopy. Survey NIR spectra of AFs 5, 10, 15, and 20 in addition to ULSD are shown in Figure 9. The curves in this figure are arranged in the same order as the Raman spectra in Figure 2 and are similarly offset along the vertical axis for clarity. In general, combination and overtone transitions produce bands in NIR hydrocarbon spectra; the middle group of bands in Figure 9 arises from combinations of stretching and bending vibrations, while the first and third groups are due to C–H stretching overtones. The positions and assignments of these bands are summarized in Table 5. Because the NIR bands tend to be more diffuse than their mid-infrared counterparts (not investigated in this work), the frequencies in Table 5 are rounded to the nearest five-wavenumber interval for simplicity. Curve fitting was not undertaken for these spectra. As shown in the inset to Figure 9, there are a few similarities

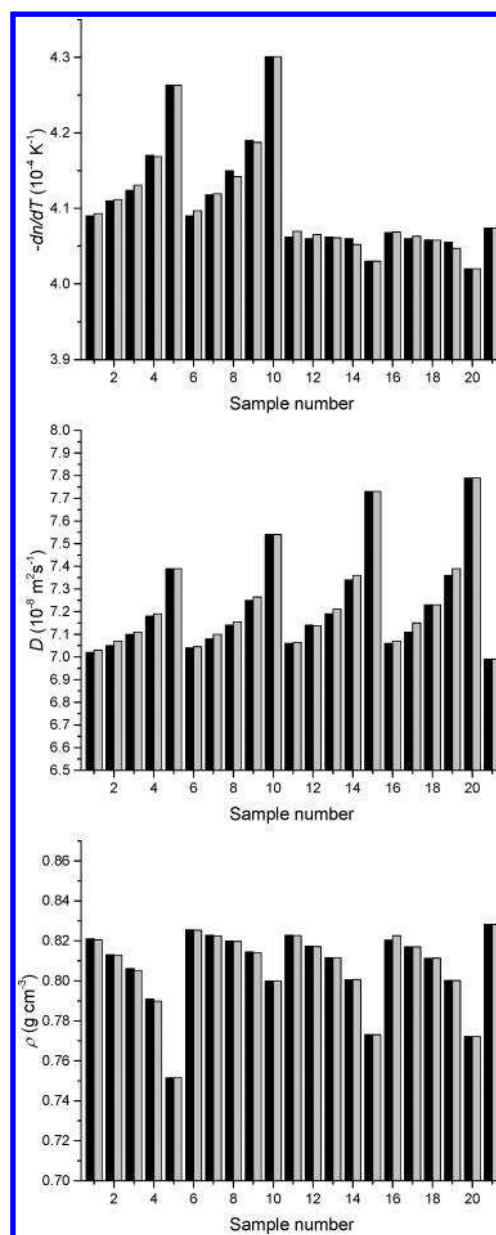


Figure 8. Comparison of experimental (black bars) and calculated (gray bars) values for $-dn/dT$ (top graph), D (middle), and ρ (bottom).

between the first overtone bands in the NIR spectra and the C–H stretching region of the Raman spectra in Figures 2–4.

3.4.1. Principal Component Analysis. PCA was applied in the 4740–8870 cm^{-1} region of the NIR spectra. As mentioned in section 2.6, the spectra were baseline linearized and mean centered prior to the PCA calculation. The first two principal components describe 64.99% and 27.95% of the data variance, respectively; while the 92.9% total is 1% higher than the

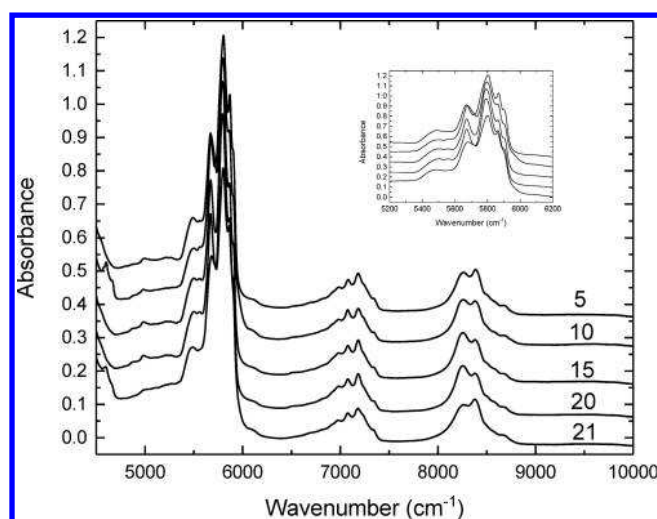


Figure 9. Near-infrared spectra of alternative fuels 5, 10, 15 and 20, as well as ULSD (sample 21). Curves are displaced vertically by successive 0.1 absorbance units for clarity. (Inset) Expanded view of C–H first overtone region, 5200–6200 cm^{-1} .

Table 5. Near-Infrared Band Assignments for AF-ULSD Blends

transition	vibration type	ν (cm^{-1})
first overtone	CH_2 symmetric stretch	5675
	CH_3 symmetric stretch	~ 5710
	CH_2 asymmetric stretch	5805
	CH_3 asymmetric stretch	5870
second overtone	aromatic CH stretch	5905
	CH_2 symmetric stretch	5950
	CH_3 symmetric stretch	8505
	CH_2 asymmetric stretch	8675
combination	CH_3 asymmetric stretch	8265
	CH_2 symmetric stretch + bend	7185
	CH_3 symmetric stretch + bend	7080

corresponding Raman result mentioned earlier, PC1 accounts for a somewhat smaller fraction of the sum in the NIR calculation.

Inspection of Figure 9 quickly leads to the suggestion that the predominant first overtone bands should account for most of the variance in PC1 and PC2.

Figure 10 shows the scores plot for the first two principal components in the NIR spectra. The scattering profile is an approximate mirror image of that in Figure 5 and again indicates the close similarities of the respective AF3 and AF4 blends. Three distinct groups, labeled in the same way as in Figure 5, are visible in Figure 10. For PC1, AF3 and AF4 (region B) exhibit the highest positive values, followed by AF1 (region A). The AF2 blends produce negative data, and ULSD is the most negative of all. A different sequence is observed for PC2: AF2 is the most positive; AF3, AF4, and ULSD are near zero; and AF1 is the most negative. Generally, the interpretations of PC1 and PC2 are similar to those in section 3.2.3 for the Raman data.

Loadings plots for PC1 and PC2 in addition to the observed NIR spectra for AF1–4 and ULSD are illustrated in Figure 11. As expected, the first overtone bands between about 5500 and 6000 cm^{-1} yield the largest loading magnitudes. The second overtones make a smaller contribution, and the combinations are least important. As is the case in Figure 7, the complex

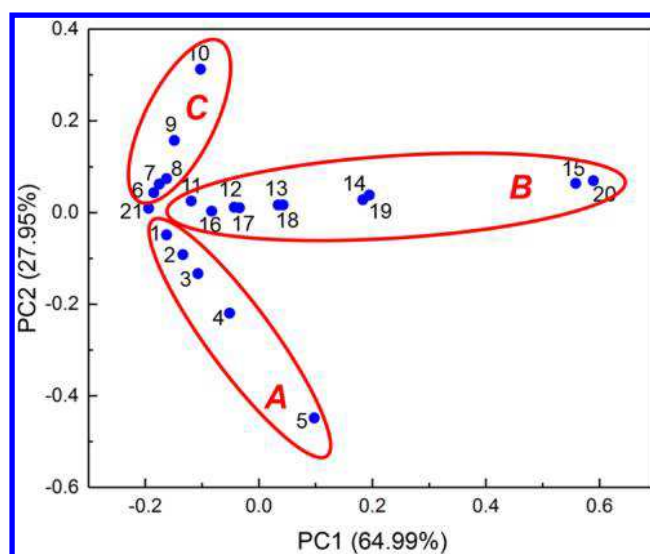


Figure 10. Scores plot using the first two principal components for the near-infrared spectra. Regions indicate fuel sets: A (samples 1–5); B (samples 11–15 and 16–20); C (samples 6–10).

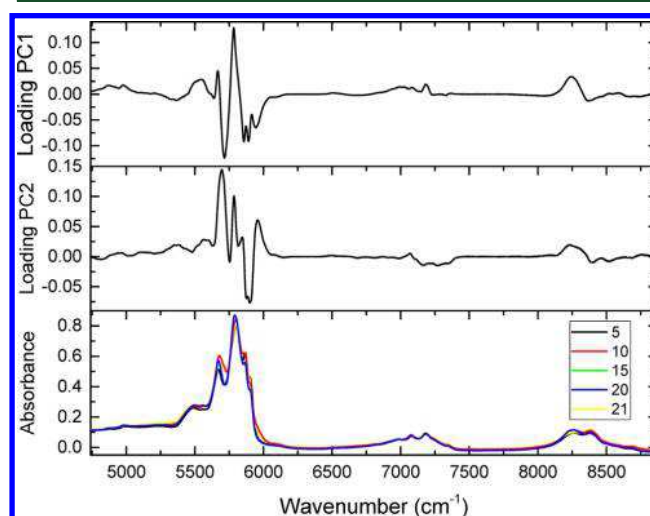


Figure 11. Near-infrared spectra for samples 5, 10, 15, 20, and 21: (top) PC1; (middle) PC2; (bottom) absorbance spectra.

positive and negative directionalities of PC1 and PC2 for the C–H stretching bands make it impossible to recognize most of the individual bands in the loading profiles.

3.3.2. PLSR. The multivariate calibration for the NIR spectra utilized the data in the entire 4740–8870 cm^{-1} region. In contrast with the analogous calculation for the Raman spectra, only three factors (variance greater than 99%) were needed for the NIR calculation. Table 6 compares the predicted and experimentally observed values for D , $-dn/dT$, and ρ for samples 1, 7, 13, and 19. The agreement is excellent, as was the case for the Raman calculations in Table 4. This confirms that NIR spectroscopy is another viable means for predicting the thermophysical properties of AF/ULSD blends.

4. CONCLUSIONS

Alternative fuel/ultralow sulfur diesel (AF/ULSD) blends, of possible interest with regard to the development of new transportation fuels, were examined in this work. Raman and NIR spectra of a series of 20 binary AF/ULSD blends were

Table 6. Actual and Predicted Values for D , $-dn/dT$, and ρ Based on NIR Data

sample	D_{actual} ($10^{-8} \text{ m}^2 \text{ s}^{-1}$)	$D_{\text{predicted}}$ ($10^{-8} \text{ m}^2 \text{ s}^{-1}$)	dn/dT_{actual} (10^{-4} K^{-1})	$dn/dT_{\text{predicted}}$ (10^{-4} K^{-1})	ρ_{actual} (g cm^{-3})	$\rho_{\text{predicted}}$ (g cm^{-3})
1	7.02	7.02	4.09	4.09	0.821	0.820
7	7.08	7.09	4.12	4.12	0.823	0.823
13	7.19	7.21	4.06	4.06	0.812	0.811
19	7.36	7.37	4.06	4.05	0.800	0.800

analyzed in detail in this study. Thermophysical (thermal diffusivity, thermo-optic coefficient) and physical (density) measurements were performed for the same blends. The spectra exhibited systematic changes in Raman band positions and intensities as the proportions of AF and ULSD varied from one blend to the next. Two AFs were found to have similar compositions. Another AF and ULSD were the only samples containing aromatic species. Trends in Raman intensities and band positions as well as thermophysical properties suggested that the AF n /ULSD blends resembled two-component mixtures despite the known complexities of the constituents. The AF and ULSD spectra combined according to the percentages of the components in each mixture. AF and ULSD thermophysical properties were similarly additive.

Numerical and chemometric methods were used to analyze the spectroscopy, thermophysical, and physical data. Both Raman and NIR spectra showed strong correlations with all three measured physical properties. Calculations confirmed that essential information is conveyed by the C–H stretching bands in the Raman and NIR spectra; additionally, the fingerprint region of the Raman spectra exhibited a similar amount of information content. These spectroscopy techniques thus create the possibility for predicting thermophysical and physical properties of similar AF/ULSD blends and make their application to other fuel blends a suitable topic for future research. This work has established that the thermophysical and physical properties of the blends are governed by the chemical components of the fuels.

■ ASSOCIATED CONTENT

📄 Supporting Information

The Supporting Information is available free of charge on the ACS Publications website at DOI: 10.1021/acs.energyfuels.7b02847.

Baseline-linearized, normalized Raman spectra C–H band positions determined by curve fitting; variations in C–H band positions; curve-fitting results for samples 1–5; curve-fitting results for samples 6–10; curve-fitting results for samples 11–15; curve-fitting results for samples 16–20 (PDF)

■ AUTHOR INFORMATION

Corresponding Author

*E-mail: jun.shen@nrc-cnrc.gc.ca.

ORCID

Jun Shen: 0000-0001-5922-5851

Luis C. Malacarne: 0000-0002-9436-6497

Notes

The authors declare no competing financial interest.

■ ACKNOWLEDGMENTS

Financial support from the Government of Canada's ecoENERGY Innovation Initiative (ecoEII) and interdepart-

mental Program of Energy Research and Development (PERD) and financial support for T. Petrucci from Brazilian Agencies CAPES and CNPq are gratefully acknowledged.

■ REFERENCES

- (1) (a) US DOE (2015). Renewable Jet Fuel is Taking Flight; <https://www.energy.gov/eere/articles/renewable-jet-fuel-taking-flight>, retrieved June 2017. (b) Honeywell UOP, Honeywell Green Jet Fuel; <https://www.uop.com/processing-solutions/renewables/green-jet-fuel/>, retrieved June 2017. (c) Newsmax (2011), "Boeing, Embraer Back Sugar Jet-Fuel Study" <http://www.newsmax.com/SciTech/Boeing-EmbraerBackSugarJet-FuelStudy/2011/07/27/id/405040/>, retrieved June 2017. (d) National Research Council Canada (2012), NRC to Fly World's First Civil Aircraft Powered by 100% Bio Jet Fuel; http://www.nrc-cnrc.gc.ca/eng/news/releases/2012/energy_biofuel.html, retrieved June 2017.
- (2) Wang, W.-Ch.; Tao, L.; Markham, J.; Zhang, Y.; Tan, E.; Batan, L.; Warner, E.; Bidy, M. Review of Biojet Fuel Conversion Technologies. NREL/TP-5100-66291, National Renewable Energy Laboratory, July 2016.
- (3) Guo, H.; Neil, W. S.; Chippior, W.; Gieleciak, R. Effect of Renewable Fuel Components on Combustion and Emission Performance of an HCCI Engine. ASME 2014 Internal Combustion Engine Division Fall Technical Conference (ICEF 2014), Columbus, IN, USA, Oct 2014; ASME, 2014.
- (4) No, S.-Y. Application of hydrotreated vegetable oil from triglyceride based biomass to CI engines – A review. *Fuel* **2014**, *115*, 88–96.
- (5) (a) Cannella, W.; Fairbridge, C.; Gieleciak, R.; Arboleda, P.; Bays, T.; Dettman, H.; Foster, M.; Gunter, G.; Hager, D.; King, D.; Lay, C.; Lewis, S.; Luecke, J.; Sluder, S.; Zigler, B.; Natarajan, M. Advanced Alternative and Renewable Diesel Fuels: Detailed Characterization of Physical and Chemical Properties. CRC Report No. AVFL-19-2; <http://www.crcao.org/reports/recentstudies2013/AVFL-19-2/CRC%20Project%20AVFL-19-2%20Final%20Report.pdf>. (b) Gieleciak, R.; Littlejohns, J. Advanced Hydrocarbon Analysis of Low Carbon Fuels. *CanmetENERGY-CDEV-2017-0010-RT*; Natural Resources Canada, 2017.
- (6) Shen, J.; Astrath, N. G. C.; Pedreira, P. R. B.; Guimarães, F. B.; Gieleciak, R.; Wen, Q.; Michaelian, K. H.; Fairbridge, C.; Malacarne, L. C.; Rohling, J. H.; Baesso, M. L. Correlations among thermophysical properties, ignition quality, volatility, chemical composition, and kinematic viscosity of petroleum distillates. *Fuel* **2016**, *163*, 324–333.
- (7) Shen, J.; Zhou, J.; Gu, C.; Neill, S.; Michaelian, K. H.; Fairbridge, C.; Astrath, N. G. C.; Baesso, M. L. A simplified model for thermal-wave cavity self-consistent measurement of thermal diffusivity. *Rev. Sci. Instrum.* **2013**, *84*, 124902.
- (8) Steimacher, A.; Medina, A. N.; Bento, A. C.; Rohling, J. R.; Baesso, M. L.; Reynoso, V. C. S.; Lima, S. M.; Petrovich, M. N.; Hewak, D. W. The temperature coefficient of the optical path length as a function of the temperature in different optical glasses. *J. Non-Cryst. Solids* **2004**, *348*, 240–244.
- (9) Jolliffe, I. T. *Principal Component Analysis*, 2nd ed.; Springer-Verlag: New York, 2002.
- (10) Martens, H.; Naes, T. *Multivariate Calibration*; John Wiley & Sons Ltd.: United Kingdom, 1989.
- (11) Stone, M. Cross-Validatory Choice and Assessment of Statistical Predictions. *J. R. Stat. Soc. B* **1974**, *36*, 111–147.

(12) Michaelian, K. H.; Hall, R. H.; Bulmer, J. T. FT-Raman and photoacoustic infrared spectroscopy of Syncrude heavy gas oil distillation fractions. *Spectrochim. Acta, Part A* **2003**, *59*, 811–824.

(13) Michaelian, K. H.; Hall, R. H.; Bulmer, J. T. FT-Raman and photoacoustic infrared spectroscopy of Syncrude light gas oil distillation fractions. *Spectrochim. Acta, Part A* **2003**, *59*, 2971–2984.

(14) Corsetti, S.; Zehentbauer, F. M.; McGloin, D.; Kiefer, J. Characterization of gasoline/ethanol blends by infrared and excess infrared spectroscopy. *Fuel* **2015**, *141*, 136–142.

(15) Corsetti, S.; McGloin, D.; Kiefer, J. Comparison of Raman and IR spectroscopy for quantitative analysis of gasoline/ethanol blends. *Fuel* **2016**, *166*, 488–494.

(16) Wen, Q.; Shen, J.; Shi, Z.; Dy, E.; Michaelian, K. H.; Fairbridge, C.; Astrath, N. G. C.; Rohling, J. H.; Baesso, M. L. Temperature coefficients of the refractive index for hydrocarbons and binary mixtures. *Chem. Phys. Lett.* **2012**, *539–540*, 54–57.

(17) Wen, Q.; Shen, J.; Gieleciak, R.; Michaelian, K. H.; Rohling, J. R.; Astrath, N. G. C.; Baesso, M. L. Temperature Coefficients of the Refractive Index for Complex Hydrocarbon Mixtures. *Int. J. Thermophys.* **2014**, *35*, 930–941.